Supplementary Material

Boosting hydrogen evolution through hydrogen spillover promoted by Co-based support effect

Ya-Nan Zhou [a], Xin Liu [a], Cheng-Jie Yu [a], Bin Dong [*a], Guan-Qun Han [b], Hai-Jun Liu [a],

Ren-Qing Lv [a], Bin Liu [a], Yong-Ming Chai [*a]

a State Key Laboratory of Heavy Oil Processing, College of Chemistry & Chemical Engineering,

China University of Petroleum (East China), Qingdao 266580, PR China

b Department of Chemistry, University of Cincinnati, Cincinnati, Ohio 45221, United States

* Corresponding author. Email: dongbin@upc.edu.cn (B. Dong); ymchai@upc.edu.cn (Y.M. Chai)

Tel: +86-532-86981156, Fax: +86-532-86981156

Characterization

SEM (JEM 2100F) and TEM (FEI Tecni G20, 200 kV) were used to characterize the morphology information of all the synthesized samples. The crystal structure of the samples is collected by means of X-ray diffraction (XRD) with Cu Kα radiation (λ = 1.54 Å) on the Brook D8 advance equipment. Energy-dispersive X-ray spectroscopy (EDS) is applied on the Hitachi S-4800 to obtain the elemental composition and distribution of the resulting sample. X-ray photoelectron spectroscopy (XPS) is employed to analyze the surface chemical structure and valence information by Thermo Fisher K-alpha 250Xi. Work function determination was derived from ultraviolet photoelectron spectroscopy (UPS, ESCALAB 250 Xi spectrometer).

Electrochemical measurements

Electrochemical performance measurements were performed at room temperature by a standard three-electrode system with Gamry Reference 3000 electrochemical equipment. The cut Ni foam (NF) (1 cm × 2 cm) was ultrasonically treated with hydrochloric acid, acetone, ethanol and deionized water, respectively, for 30 min to remove the surface impurity. All electrochemical measurements were conducted under the same conditions in 0.5 M H_2SO_4 or 1.0 M KOH. The obtained samples grown on NF (effective electrode area is 2 cm^2), graphite rod electrode and saturated calomel electrode (0.5 M H_2SO_4)/Hg/HgO electrode (1.0 M KOH) were selected as working electrode, counter electrode and reference electrode, respectively. The scan rate of linear sweep voltammetry (LSV) curves was 5 mV s^{-1}. In the test process, positive feedback method is used to conduct IR compensate in real time (95%). All the electrode potentials were converted to reversible hydrogen electrode (RHE) via the Nernst

equation: $E_{RHE} = E_{SCE} + 0.0592\ pH + E^0_{SCE}$ ($E^0_{SCE} = 0.245$ V, $E^0_{Hg/HgO} = 0.098$ V). The CV curves with different scanning rates (40, 60, 80, 100 and 120 mV S^{-1}) are employed to determine the double-layer capacitances (C_{dl}). Electrochemical active surface area (ECSA) was calculated by calculating the current difference at a specific voltage in the non-Faraday region. The stability of the sample was evaluated via both chronoamperometry (at 50 mA cm^{-2}) and fast CV cycles with a rate of 40 mV s^{-1} for 3000 sweeps. The frequency of electrochemical impedance spectroscopy (EIS) was gained at a certain potential ranging from 10^5 Hz to 0.1 Hz with an AC voltage of 5 mV. All the (over)potentials in this work are converted to RHE unless otherwise noted.

TOF calculation

To calculate the per-site turnover frequency (TOF), we used the following formula:

$$TOF = \frac{total\ hydrogen\ turnovers/cm^2\ geometric\ area}{active\ sites/cm^2\ geometric\ area}$$

The total number of hydrogen turn overs was calculated from the current density according to[29-31]:

$$H_2 = \left(j\frac{mA}{cm^2}\right)\left(\frac{1\ C\ s^{-1}}{1000\ mA}\right)\left(\frac{1\ mol\ e^-}{96485.3\ C}\right)\left(\frac{1\ mol\ H_2}{2\ mol\ e^-}\right)\left(\frac{6.022\times10^{23}\ H_2\ mo}{1\ mol\ H_2}\right)$$

$$\frac{H_2/s}{cm^2} per \frac{mA}{cm^2}$$

Since the exact hydrogen binding site is not known, we estimate the number of active sites as the number of surface Co sites, from the roughness factor together with the unit cell of the CoP/CoO_x/CoS_x/$CoSe_2$ and Pt-CoP/CoO_x/CoS_x/$CoSe_2$. Taking CoP (volume: 89.84 $Å^3$, containing 3 Co atoms) as an example:

Active sites per surface area:

$$active\ sites = \left(\frac{3\ atoms/unit\ cell}{89.84\ Å^3/unit\ cell}\right)^{\frac{2}{3}} = 1.04 \times 10^{15}\ atoms\ cm_{real}^{-2}$$

Finally, plots of current density can be converted into a TOF plot according to:

$$TOF = \frac{\left(3.12 \times 10^{15} \frac{H_2/s}{cm^2}\ per\ \frac{mA}{cm^2}\right) \times |j|}{\left(1.69 \times 10^{15}\ atoms/cm_{real}^2\right) \times A_{ECSA}}$$

A similar approach was used to estimate TOF for other samples.

DFT calculation

According to XRD patterns, the typical, well-crystallized and unadulterated CoP and Co_3O_4 were chosen as the objects to study the hydrogen spillover process. The whole modeling process refers to the published literature.[32,33] The crystal surface of (011) and (210) was chosen for CoP and Co_3O_4 according to XRD and TEM results. In the calculations, the Pt cluster was built on the CoP (011) and Co_3O_4 (210) surface with a vacuum region of 20 Å to reduce dispersive error. The optimized Pt/CoP and Pt-Co_3O_4 geometries are shown in Fig. S21. During the interface optimization, single point energy was used to optimize the distance between Pt clusters and CoP/Co_3O_4, then bottom layer of metals and CoP/Co_3O_4 layers were fixed in order to reduce the calculation time. The CASTEP module of the Materials Studio software was employed for the quantum chemistry calculations. Perdew-Burke-Ernzerhof Generalized-Gradient-Approximation method was used with Density Functional Dispersion correction to calculate the exchange-correlation energy. Ultrasoft pseudopotential was selected to describe the characters of ionic cores. During the interface optimization, the top one layer of CoP was relaxed in order to reduce the calculation time. The k-point is Gamma point for adsorption thermodynamics. The optimization is completed when the energy,

maximum force, maximum stress and maximum displacement are smaller than 5.0×10^{-6} $eV \cdot atom^{-1}$, 0.03 $eV \cdot Å^{-1}$, 0.02 GPa and 5.0×10^{-4} Å, respectively. Gibbs free energy of adsorption hydrogen atom are calculated by the following equation: $\Delta G_H = Esurface + H^* - Esurface - 2EH_2 + \Delta E_{ZPE} - T\Delta S_H$

where Esurface+H* is the total energy of the system, including the adsorbed molecules and facet; Esurface is the energy of the facet; EH_2 represents the total energy of a gas phase H_2 molecule; ΔE_{ZPE} denotes the zero-point energy of the system simplified as 0.05 eV; The $-T\Delta S_H$ is the contribution from entropy at temperature K, taken as 0.20 eV at 298 K.

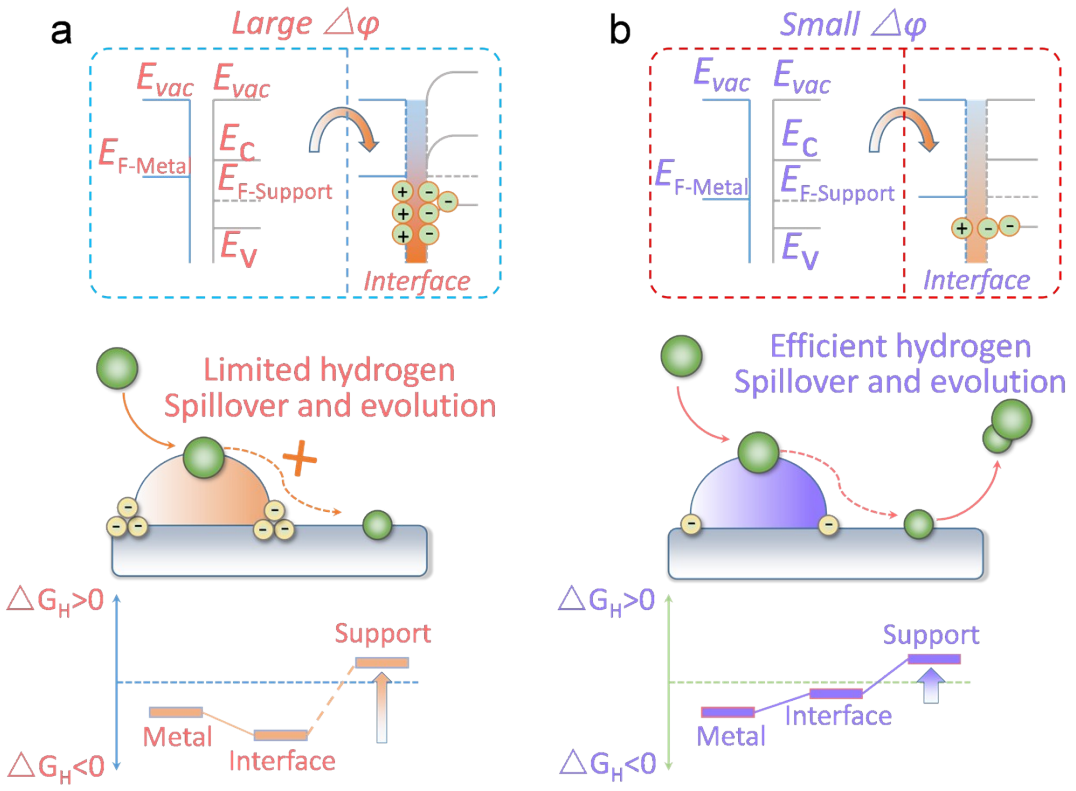

Fig. S1. Schematic illustrations of the interfacial electronic configurations and hydrogen spillover phenomenon during HER for the hydrogen-spillover-based binary electrocatalysts with (a) large ΔΦ or (b) small ΔΦ. E_{vac} = vacuum energy, E_C = conduction band, E_v = valence band, and E_F = Fermi level.

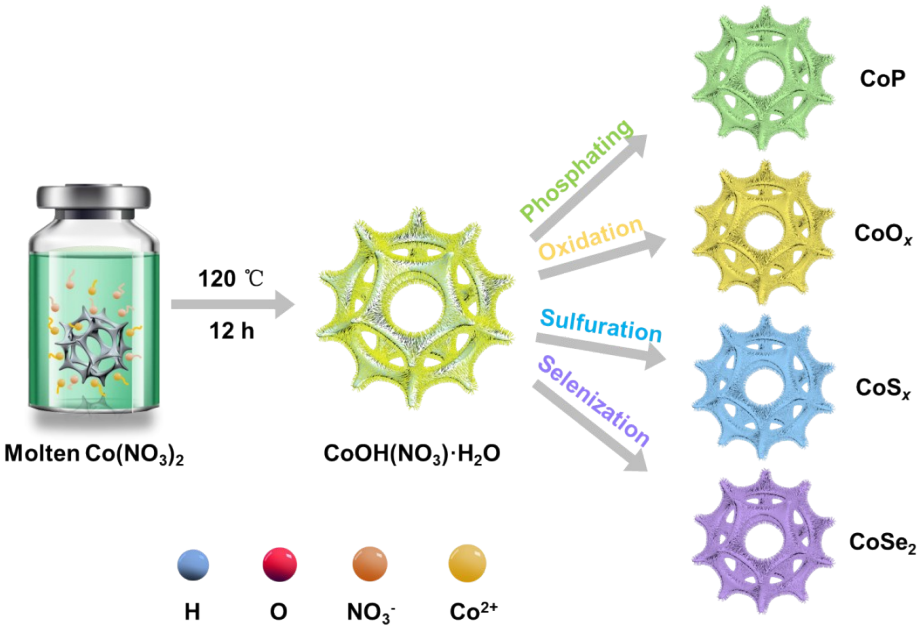

Fig. S2. Schematic illustration of the synthesis of CoP, CoO_x, CoS_x and $CoSe_2$.

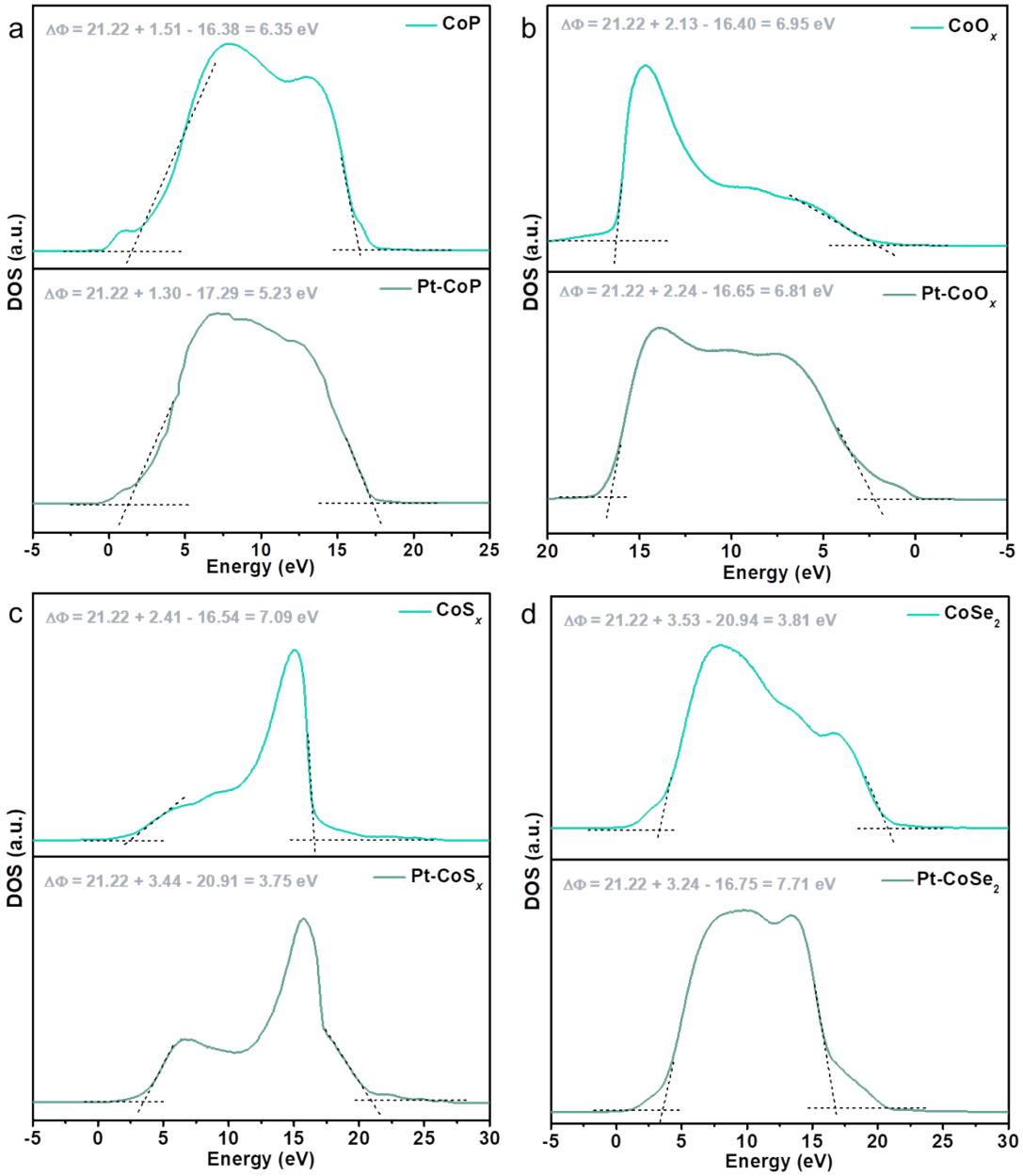

Fig. S3. Work function measurements for (a) CoP and Pt-CoP, (b) CoO_x and Pt-CoO_x, (c) CoS_x and Pt-CoS_x, (d) $CoSe_2$ and Pt-$CoSe_2$.

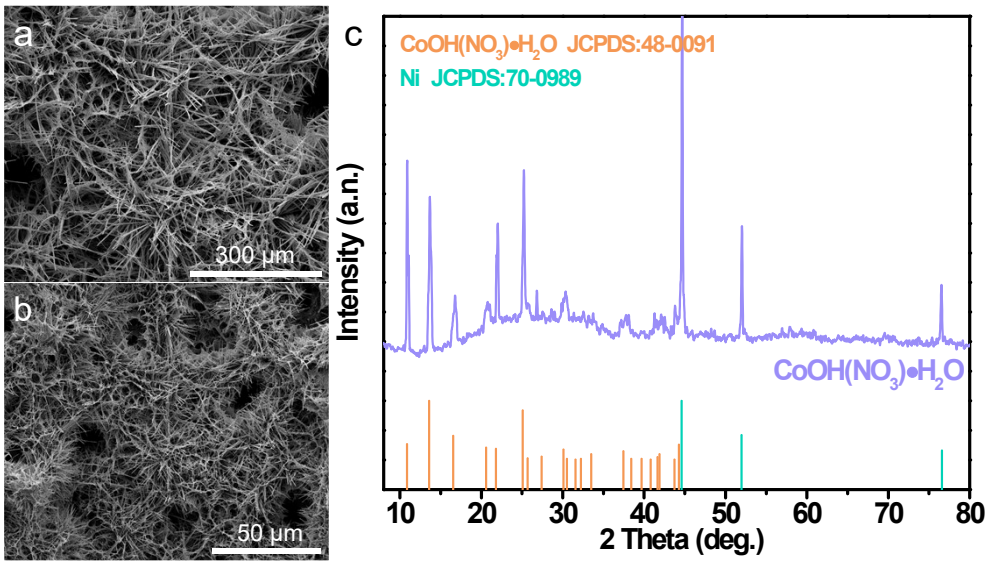

Fig. S4. (a,b) SEM images and (c) XRD pattern of $CoOH(NO_3)\cdot H_2O$. $CoOH(NO_3)\cdot H_2O$ precursor shows the nanowire structure covering the whole nickel foam.

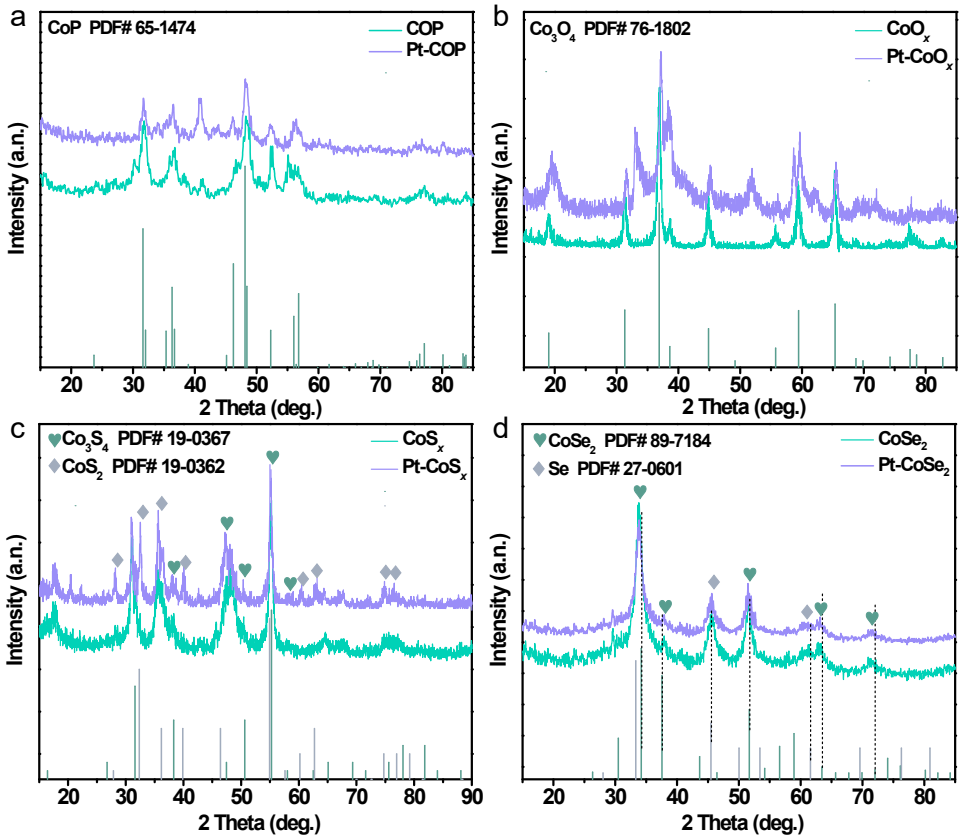

Fig. S5. XRD patterns of (a) CoP and Pt-CoP, (b) CoO_x and Pt-CoO_x, (c) CoS_x and Pt-CoS_x, (d) $CoSe_2$ and Pt-$CoSe_2$. The XRD peaks of (d) show discernible movement, which is due to the lattice distortion or stress.

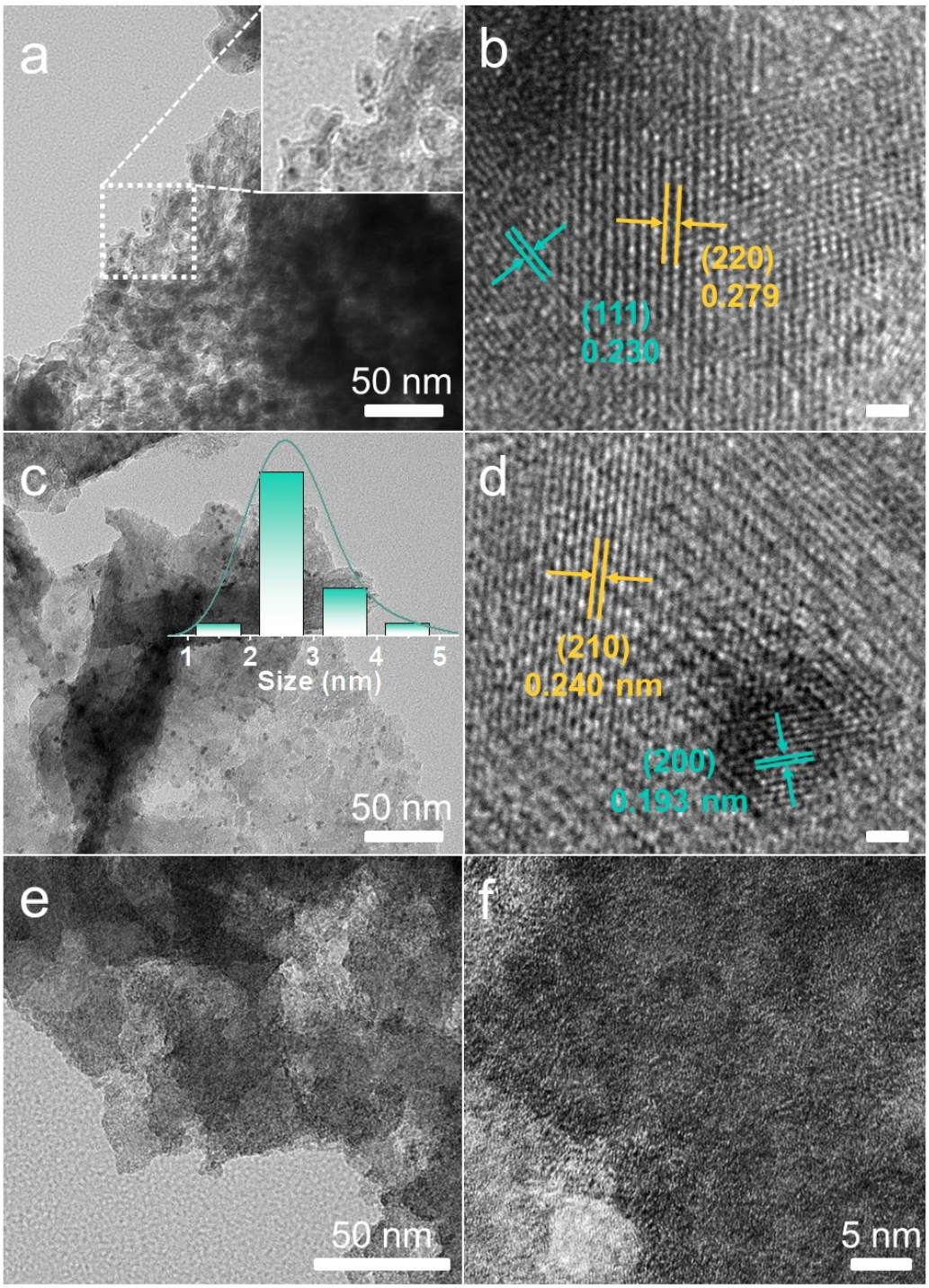

Fig. S6. TEM images of (a,b) Pt-CoO_x, (c,d) Pt-CoS_x, (e,f) Pt-$CoSe_2$ scratched off from the as-prepared NF electrode.

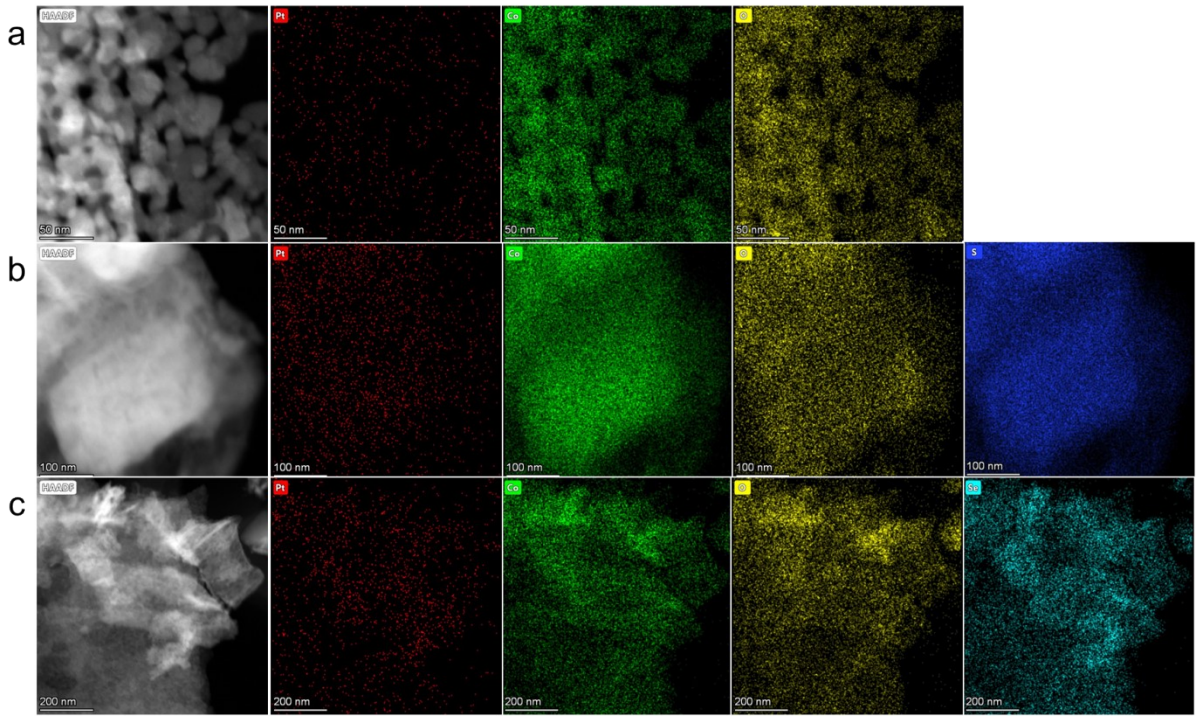

Fig. S7. Element images of (a) Pt-CoO_x, (b) Pt-CoS_x, (c) Pt-$CoSe_2$.

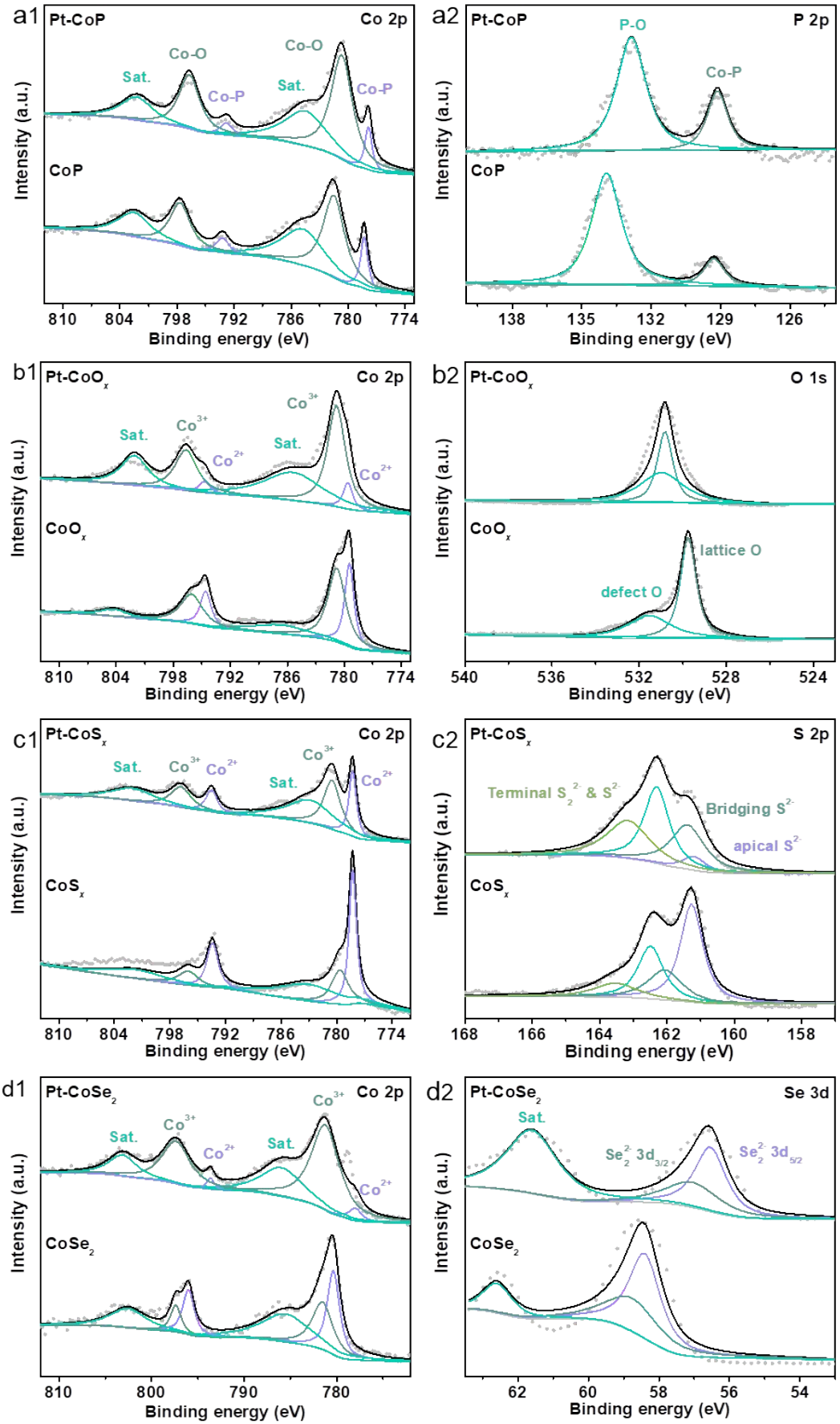
a1
Pt-CoP
Co 2p
Co-O
Co-O
Sat.
Co-P
Sat.
Co-P
CoP
Intensity (a.u.)
810 804 798 792 786 780 774
Binding energy (eV)
a2
Pt-CoP
P 2p
P-O
Co-P
CoP
Intensity (a.u.)
138 135 132 129 126
Binding energy (eV)
b1
Pt-CoO$_x$
Co 2p
Co^{3+}
Sat.
Co^{3+}
Co^{2+}
Sat.
Co^{2+}
CoO$_x$
Intensity (a.u.)
810 804 798 792 786 780 774
Binding energy (eV)
b2
Pt-CoO$_x$
O 1s
CoO$_x$
lattice O
defect O
Intensity (a.u.)
540 536 532 528 524
Binding energy (eV)
c1
Pt-CoS$_x$
Co 2p
Sat.
Co^{3+}
Co^{2+}
Sat.
Co^{3+}
Co^{2+}
CoS$_x$
Intensity (a.u.)
810 804 798 792 786 780 774
Binding energy (eV)
c2
Pt-CoS$_x$
S 2p
Terminal S$_2^{2-}$ & S^{2-}
Bridging S^{2-}
apical S^{2-}
CoS$_x$
Intensity (a.u.)
168 166 164 162 160 158
Binding energy (eV)
d1
Pt-CoSe$_2$
Co 2p
Co^{3+}
Sat.
Co^{3+}
Co^{2+}
Sat.
Co^{2+}
CoSe$_2$
Intensity (a.u.)
810 800 790 780
Binding energy (eV)
d2
Pt-CoSe$_2$
Se 3d
Sat.
Se$_2^{2-}$ 3d$_{3/2}$
Se$_2^{2-}$ 3d$_{5/2}$
CoSe$_2$
Intensity (a.u.)
62 60 58 56 54
Binding energy (eV)

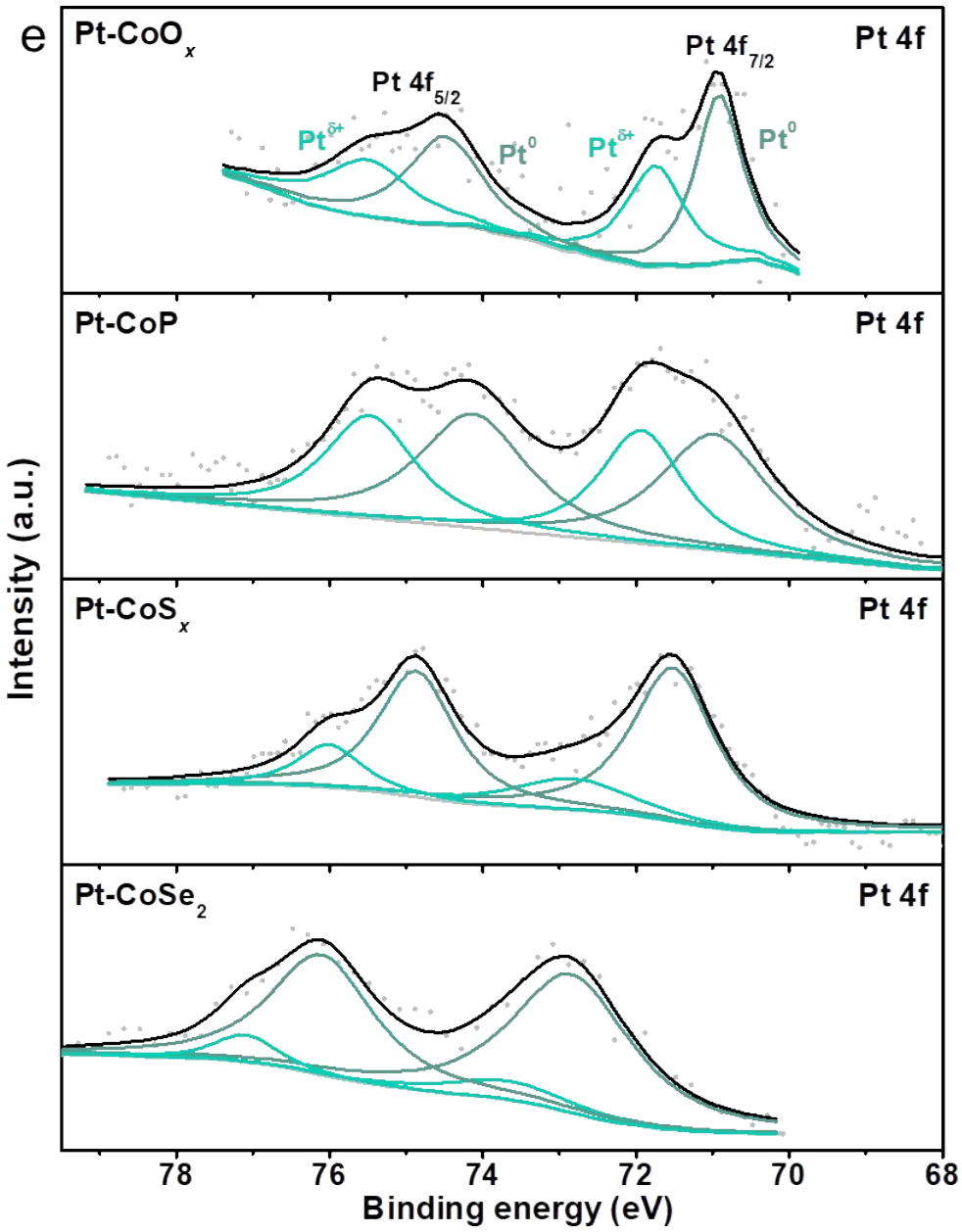

Fig. S8. (a1,a2) Co 2p and P 2p of Pt-CoP, (b1,b2) Co 2p and O 1s of Pt-CoO$_x$, (c1,c2) Co 2p and S 2p of Pt-CoS$_x$, (d1,d2) Co 2p and Se 3d of Pt-CoSe$_2$. (e) Pt 4f of various samples.

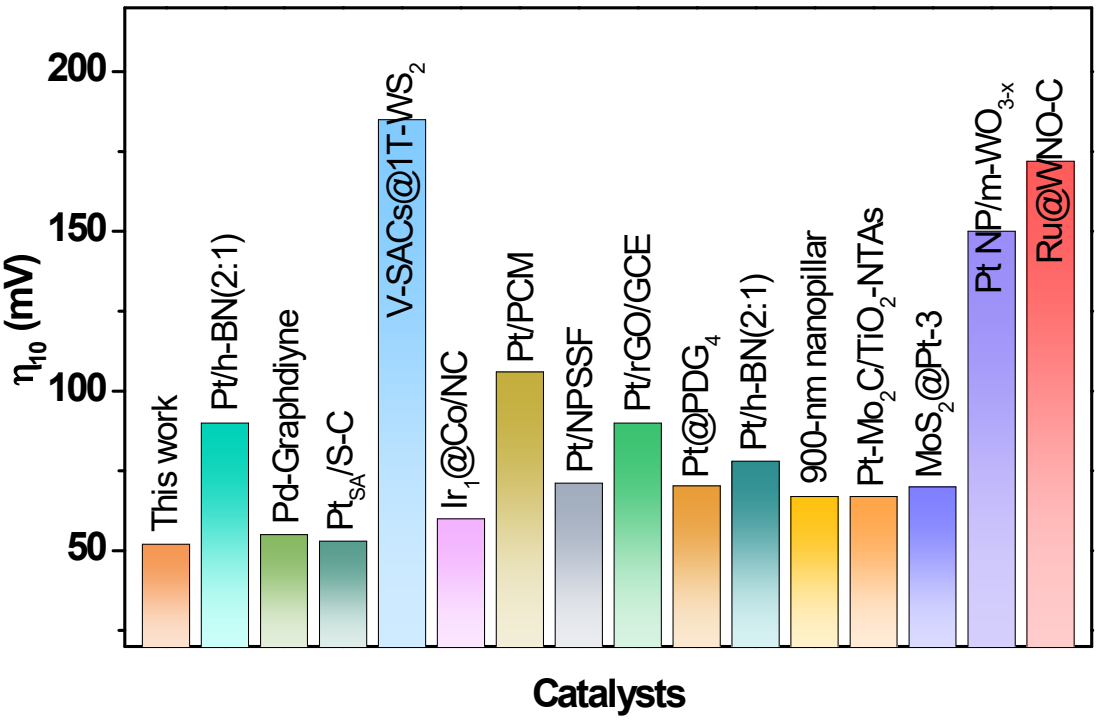

Fig. S9. Comparisons of the noble metal activity of Pt-CoP for HER with those of other well-known Pt-based catalysts from Table S2.

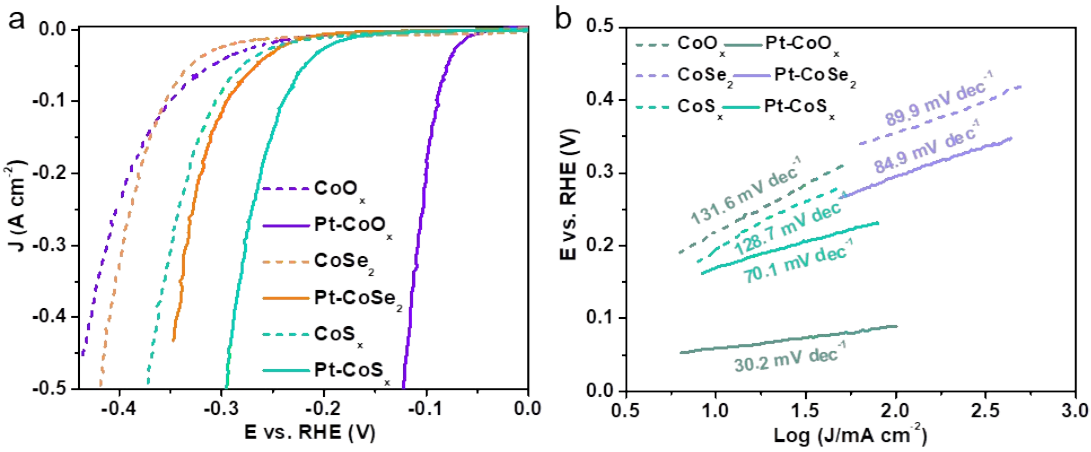

Fig. S10. (a) LSV plots and corresponding (b) Tafel slopes of CoO_x, CoS_x, $CoSe_2$, Pt-CoO_x, Pt-CoS_x and Pt-$CoSe_2$.

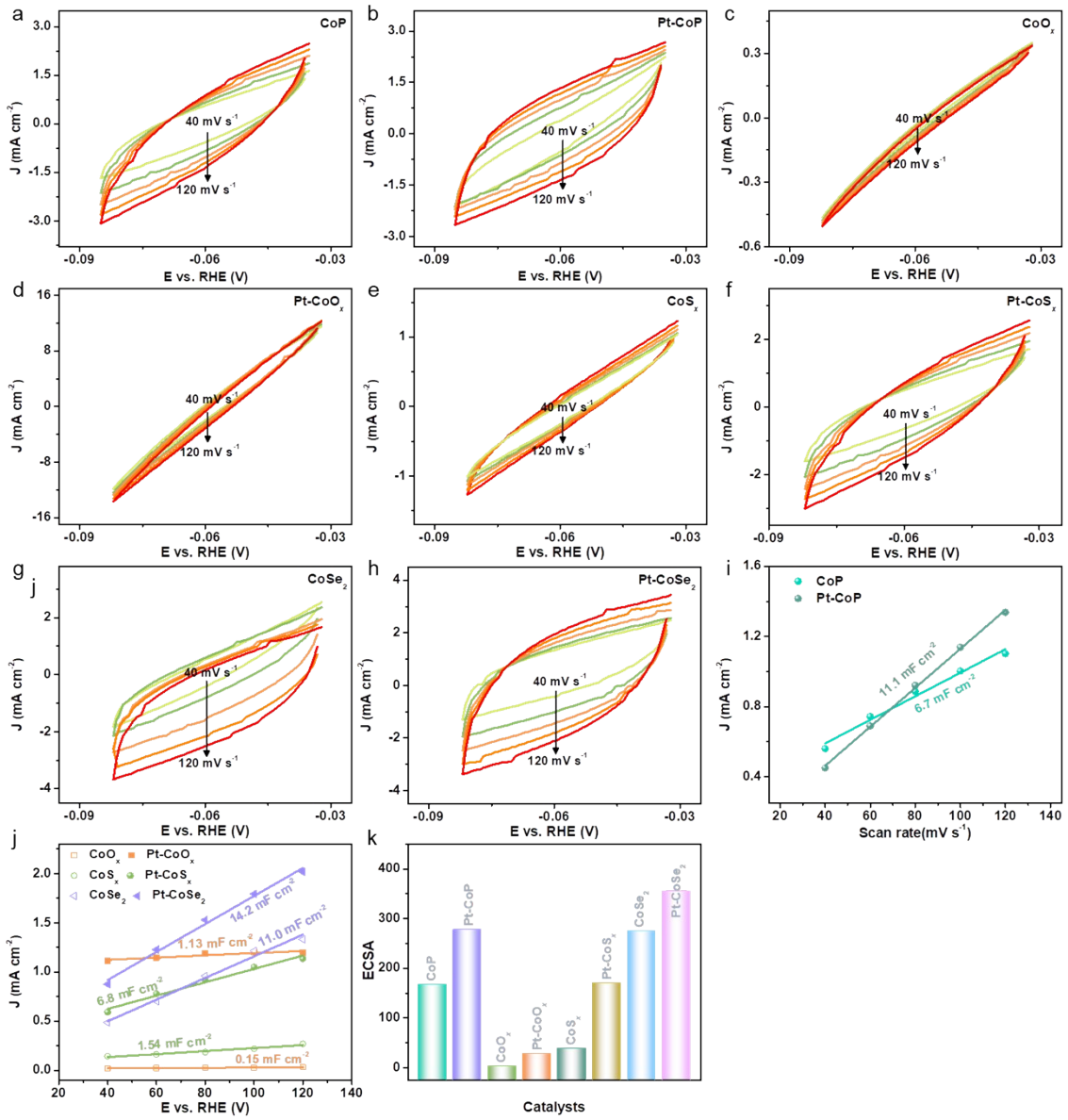

Fig. S11. CV curves of obtained samples and corresponding C_{dl} and ECSA in 0.5 M H_2SO_4.

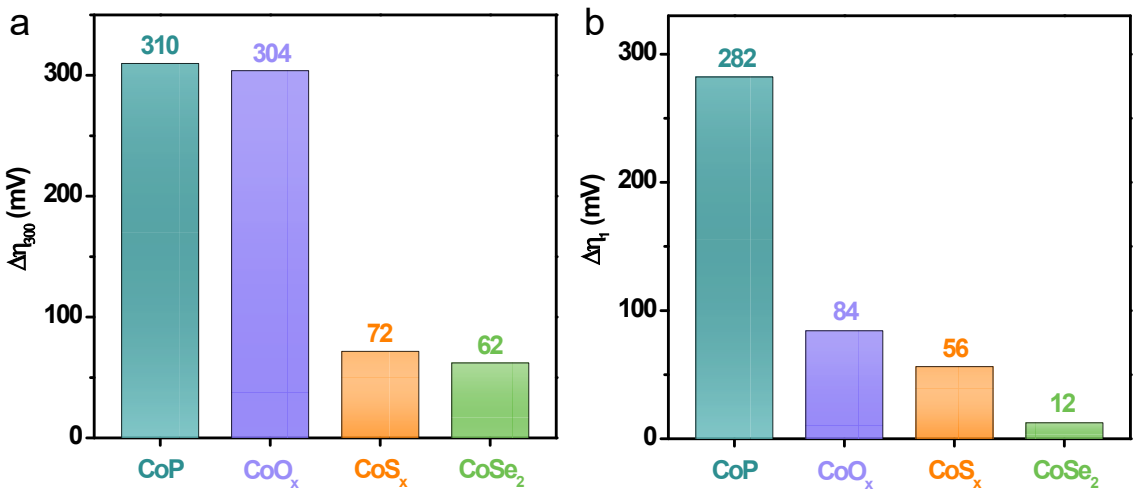

Fig. S12. Overpotential difference for CoP, CoO_x, CoS_x and $CoSe_2$ before and after Pt loading at current density of 300 mA cm^{-2} in LSV normalized by electrode area (a) and at current density of 1 mA cm^{-2} in LSV normalized by ECSA (b).

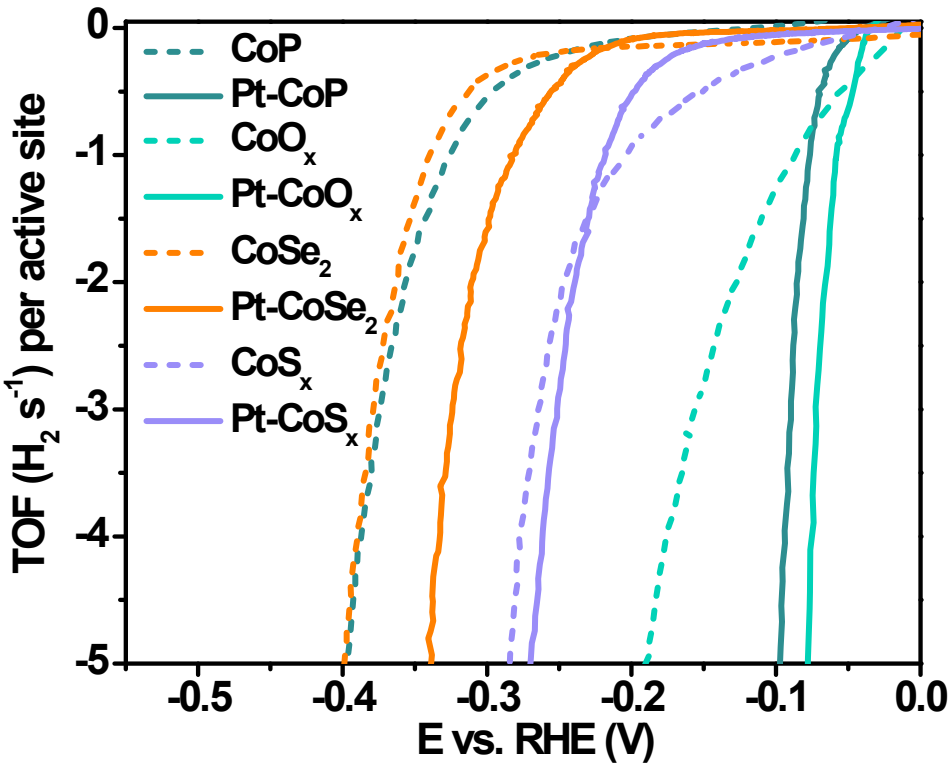

Fig. S13. TOF values of all obtained catalysts in 0.5 M H_2SO_4 solution.

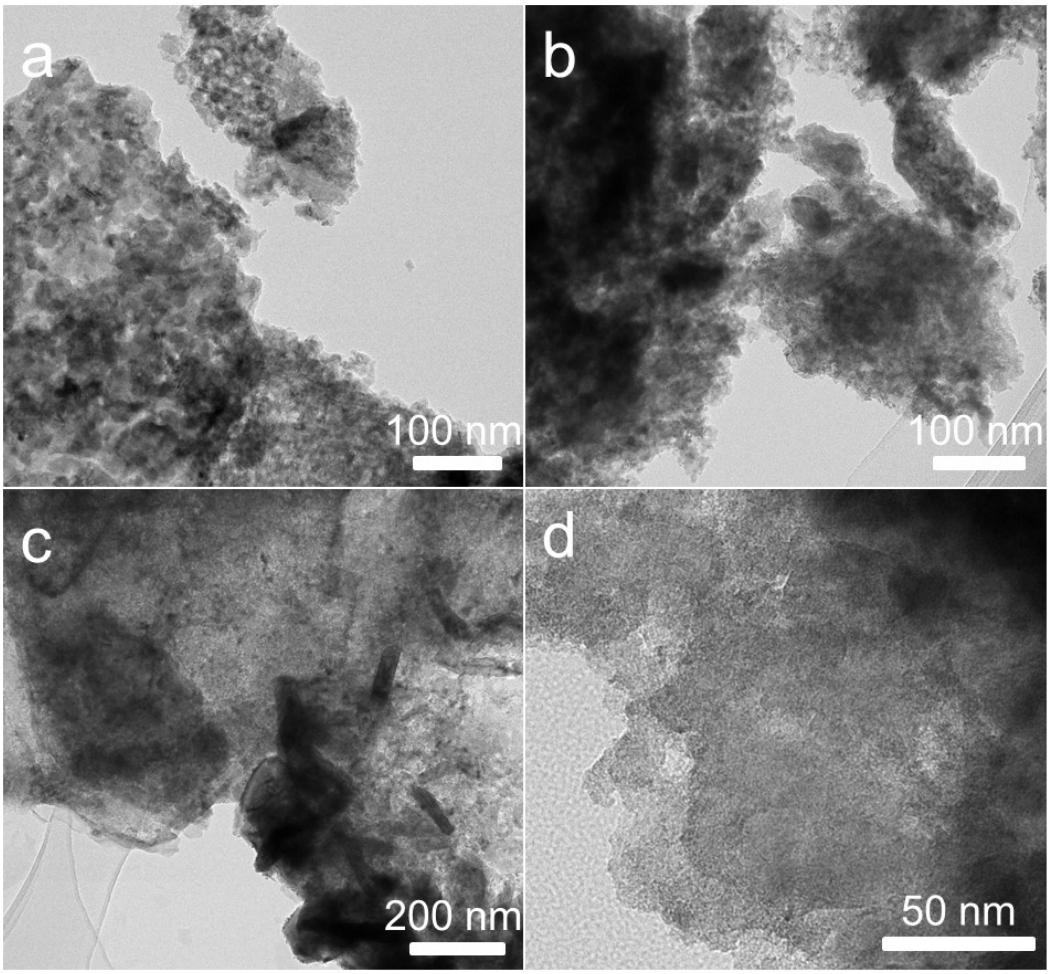

Fig. S14. TEM images of (a) Pt-CoP, (b) Pt-CoO_x, (c) Pt-CoS_x, (d) Pt-$CoSe_2$ after long-term stability in acidic media.

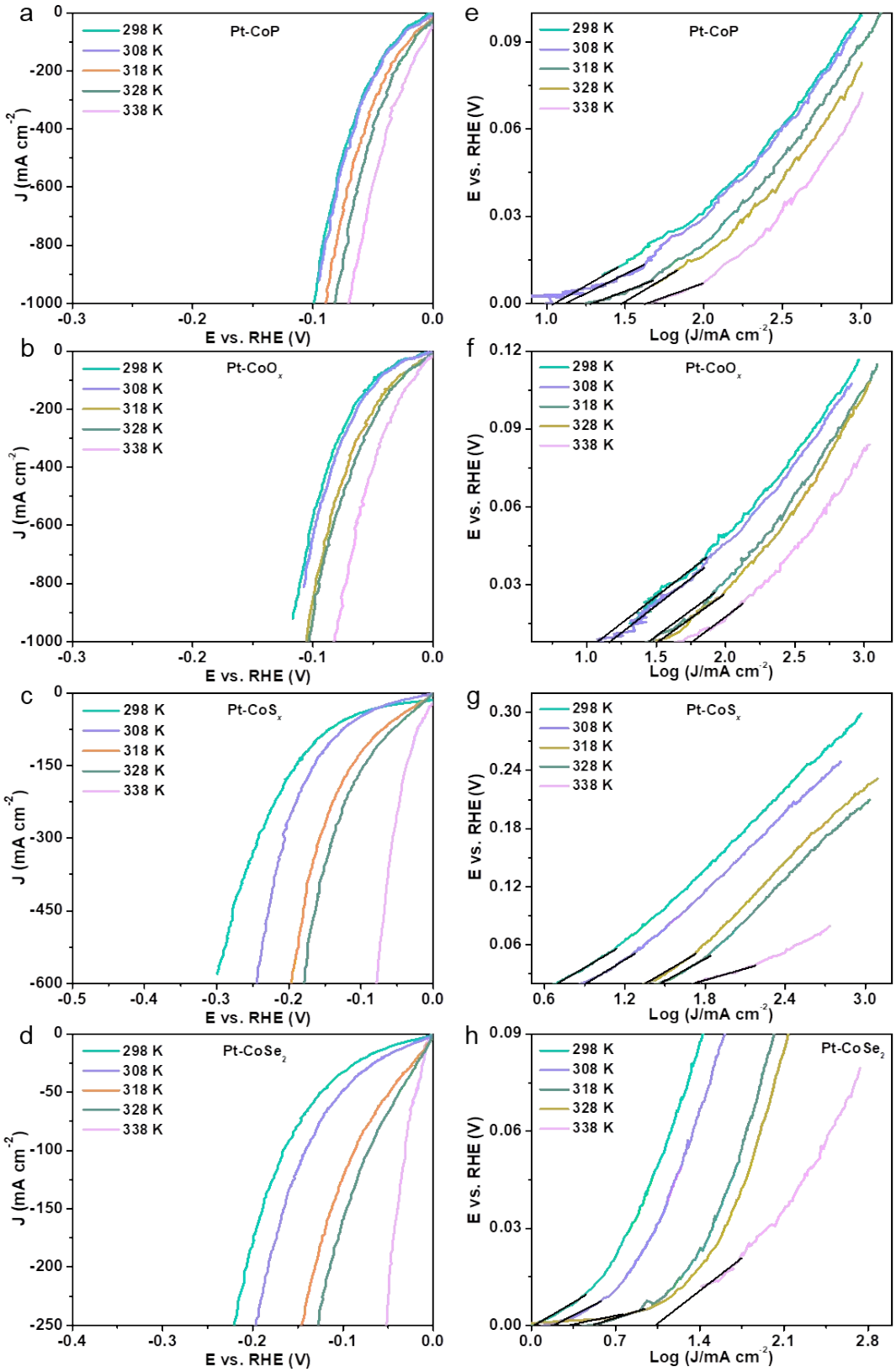

Fig. S15. (a-d) LSV curves of Pt-CoP, Pt-CoO_x, Pt-CoS_x, Pt-$CoSe_2$ and corresponding Tafel slopes in Ar-saturated 0.5 M H_2SO_4 at different temperatures from 298 to 338 K.

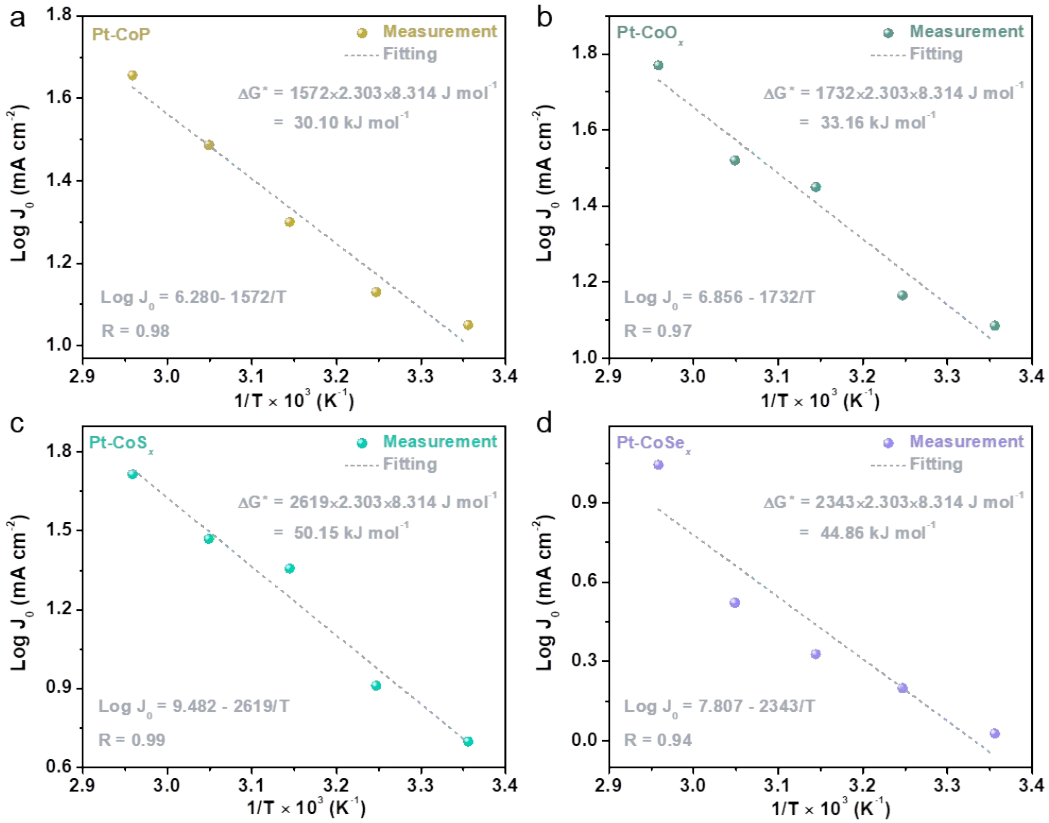

Fig. S16. Typical Arrhenius plots for the (a) Pt-CoP, (b) Pt-CoO$_x$, (c) Pt-CoS$_x$, (d) Pt-CoSe$_2$ catalysts. The calculation of the ΔG* is based on the Arrhenius equation: $\log j_0 = \log (FK_c) - \Delta G^*/2.303RT$.

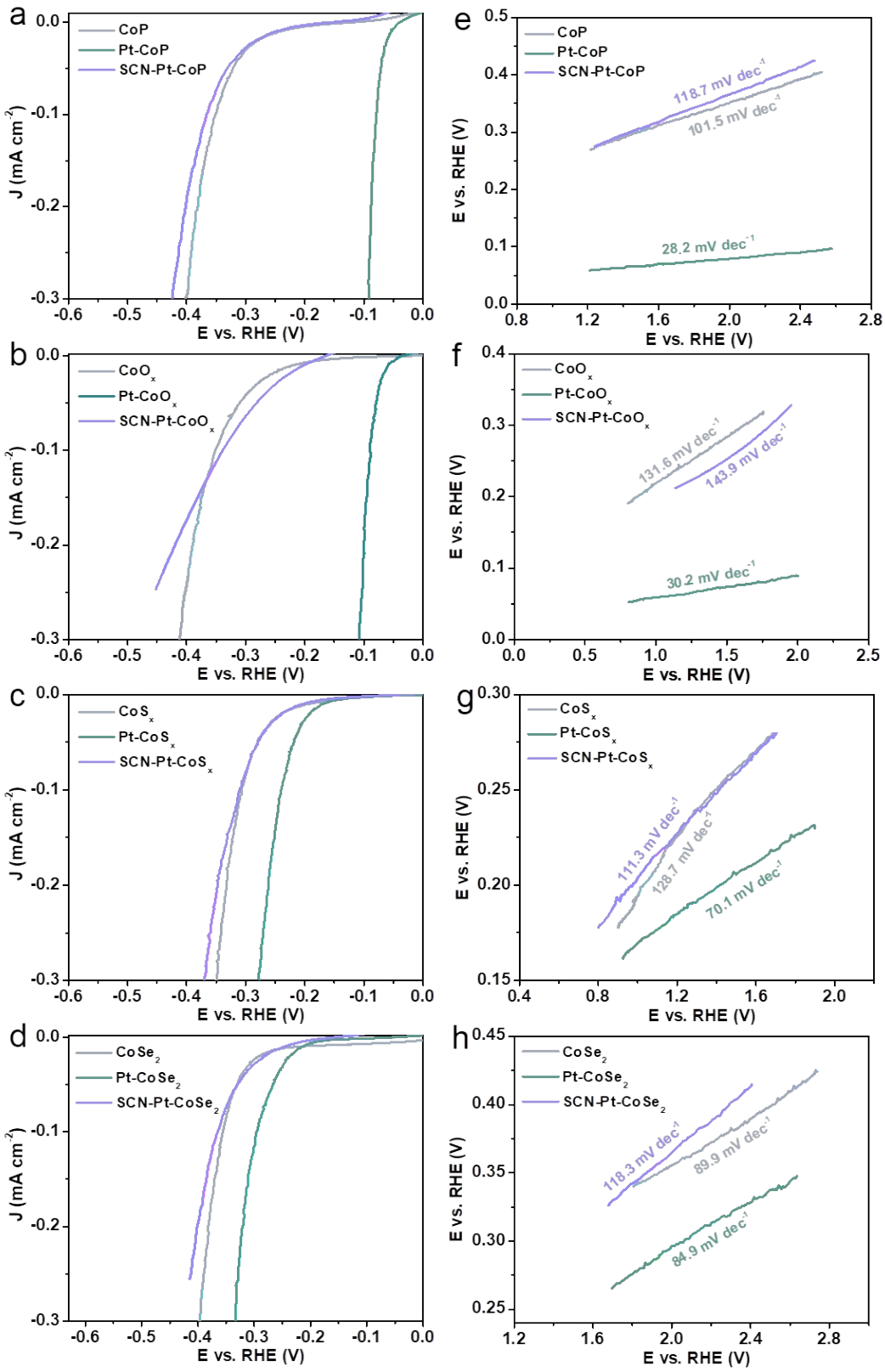

Fig. S17. HER performance of Pt-CoP, Pt-CoO_x, Pt-CoS_x, Pt-$CoSe_2$ catalysts in the presence or absence of SCN^- probe.

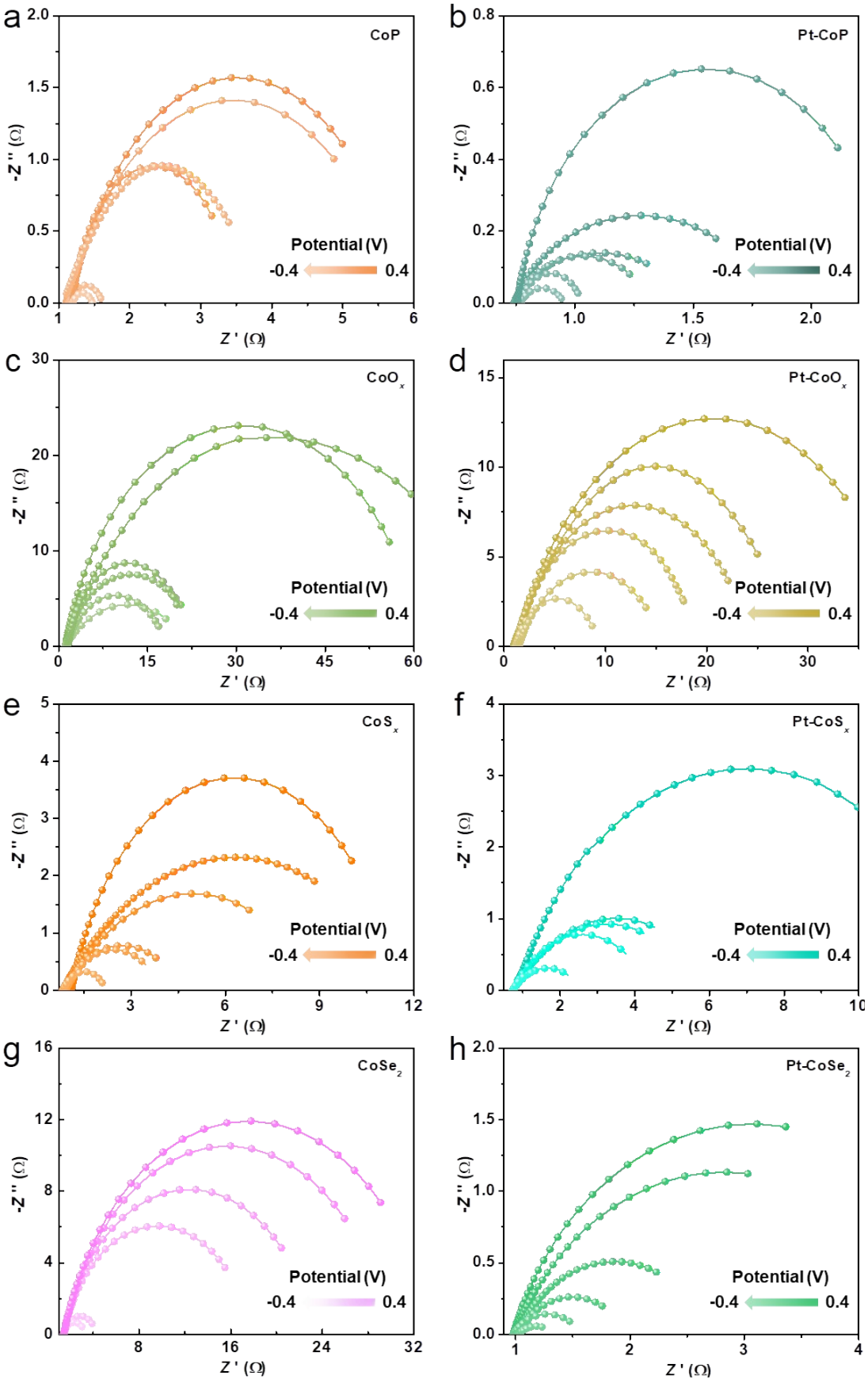

Fig. S18. EIS analysis in Ar-saturated 0.5 M H_2SO_4. Nyquist plots for obtained samples with

the model as follows:

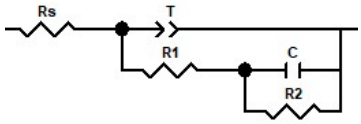

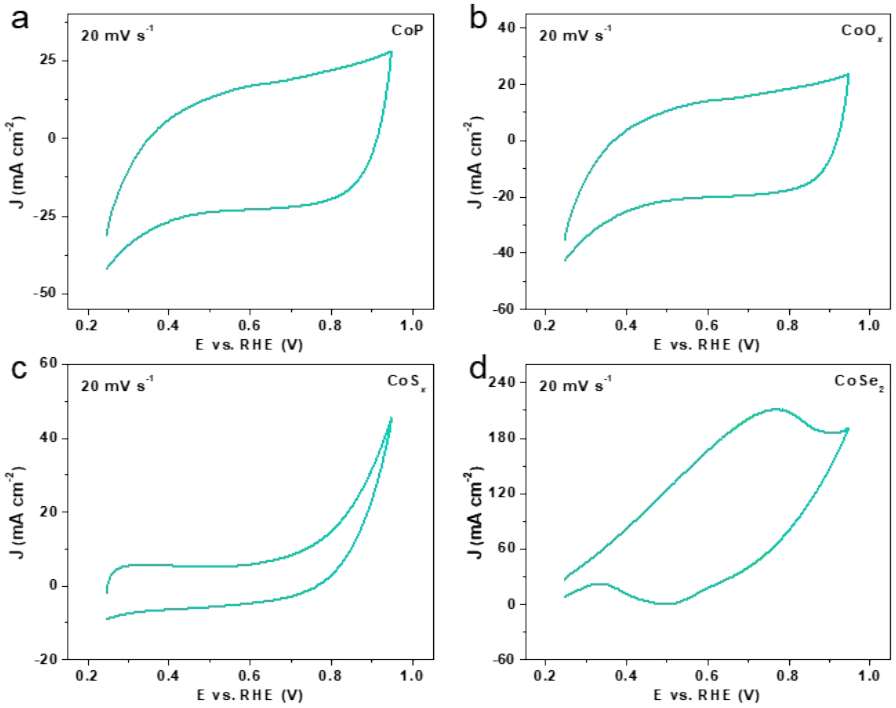

Fig. S19. CV curves of (a) CoP, (b) CoO_x, (c) CoS_x, (d) $CoSe_2$ catalysts.

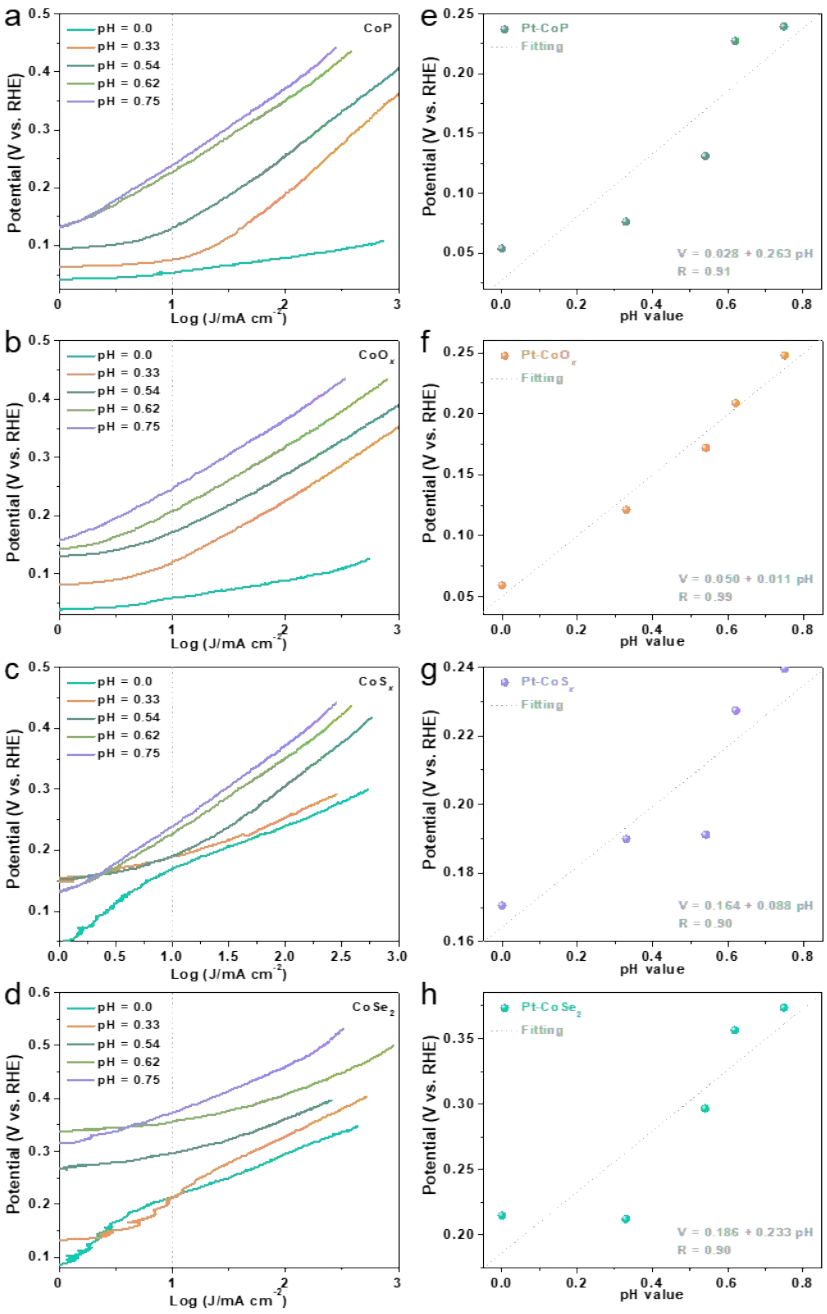

Fig. S20. (a) Tafel curves of obtained catalysts in Ar-saturated H_2SO_4 electrolyte with pH ranging from 0 to 0.75. (b) Plots of potential at 10 mA cm^{-2} vs. pH for Pt-CoP, Pt-CoO_x, Pt-CoS_x, Pt-$CoSe_2$.

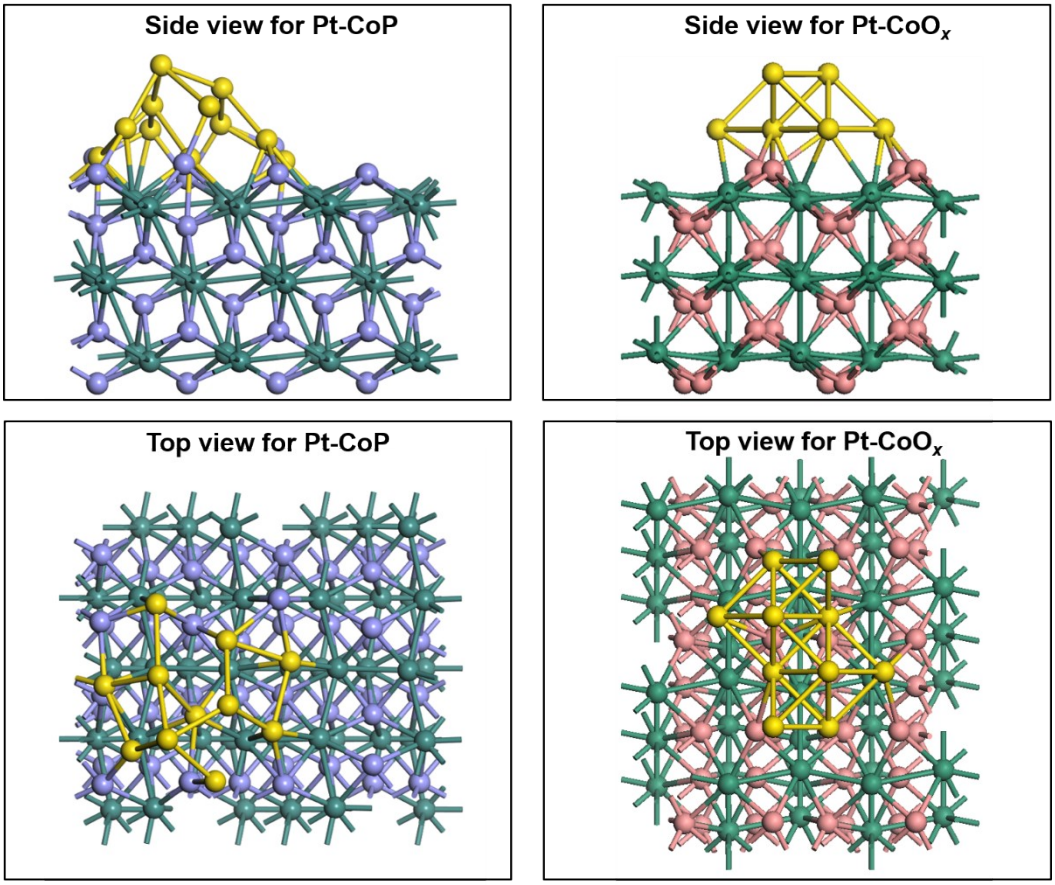

Fig. S21. Side and top view of Pt-CoP and Pt-CoO_x surfaces.

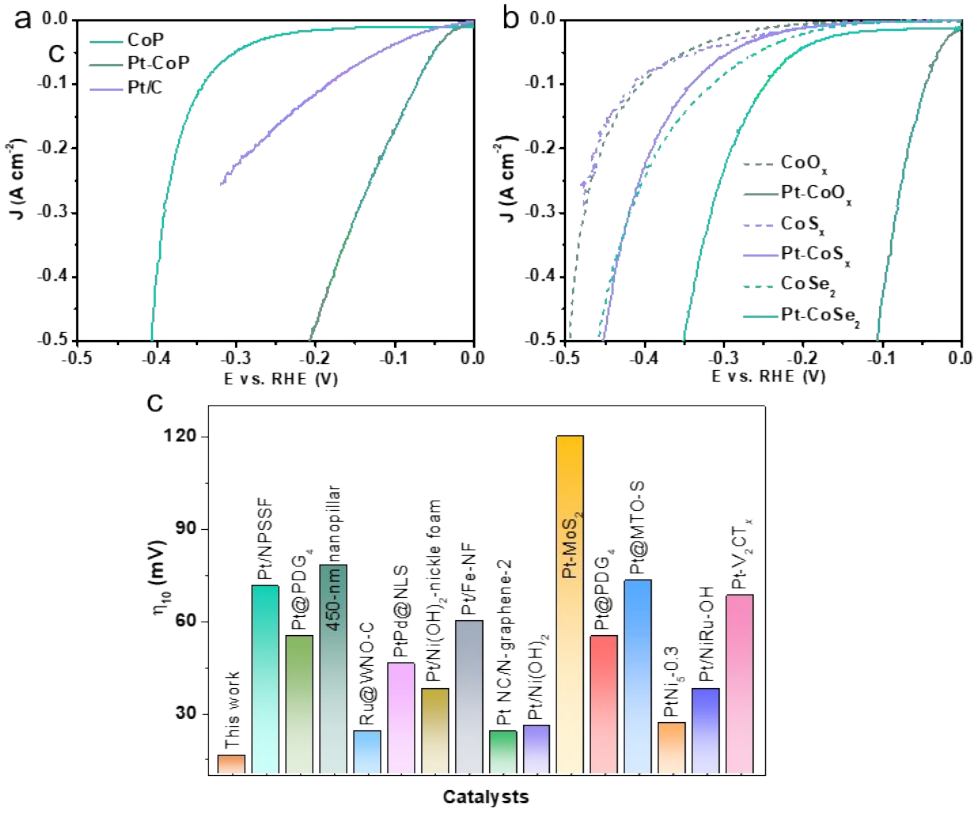

Fig. S22. HER activity of obtained catalysts in 0.5 M H_2SO_4. (a,b) LSV curves, (c) comparison of overpotential at 10 mA cm^{-2}.

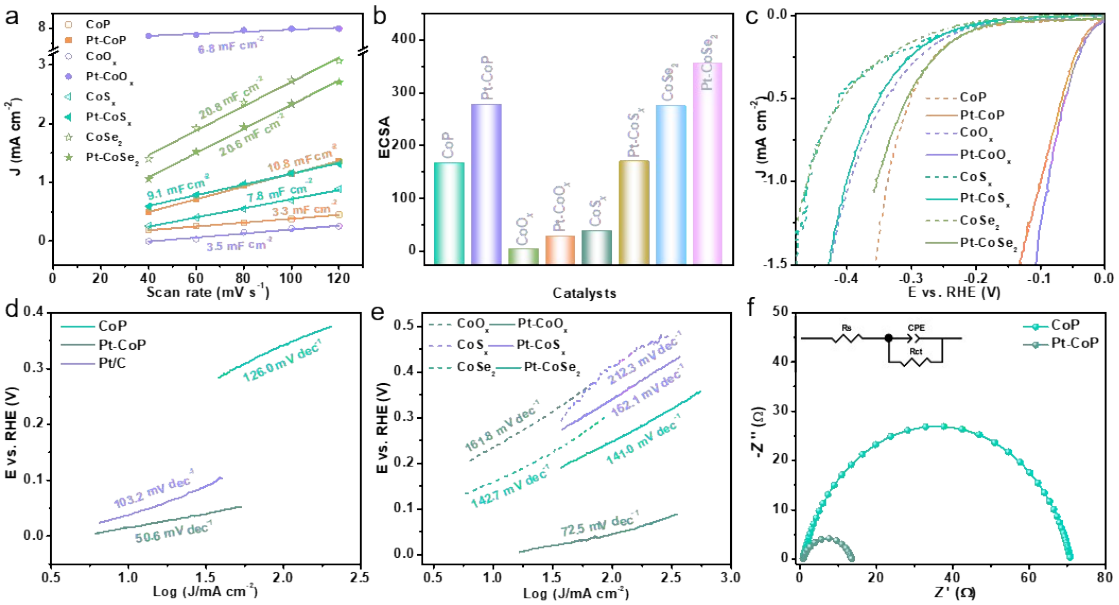

Fig. S23. HER performance of obtained catalysts in 0.5 M H_2SO_4. (a) C_{dl}, (b) ECSA, (c) ECSA-normalized LSV plots, (d,e) Tafel slopes, (f) EIS plots.

Table S1 Element contents of Pt-CoP, Pt-CoO_x, Pt-CoS_x, Pt-$CoSe_2$.

	Pt-CoP		**Pt-CoO_x**		**Pt-CoS_x**		**Pt-$CoSe_2$**	
Element	**At.%**	**Wt.%**	**At.%**	**Wt.%**	**At.%**	**Wt.%**	**At.%**	**Wt.%**
Pt	0.20	1.09	0.07	0.48	0.07	0.35	0.30	1.32
Co	34.22	57.20	32.04	63.18	32.50	48.78	25.84	33.76
P	28.12	24.70	-	-	-	-	-	-
S	-	-	-	-	57.21	46.71	-	-
O	37.46	17.00	67.88	36.34	10.21	4.16	46.11	16.36
Se	-	-	-	-	-	-	27.74	48.57

Table S2. Comparison of HER performance in acidic media for best-performing Pt/CoP with the noble-metal based catalysts.

Catalysts	**Loading of noble metal**	**η_{10} (mV)**	**Tafel slope (mV dec^{-1})**	**Reference**
Pt/CoP	0.12 at.%	52	28.2	This work
Pt/h-BN (2:1)	-	90	34	1
Pd-Graphdiyne	0.2 wt.%	55	47	2
Pt_{SA}/S-C	5.0 wt.%	53	46	3
V-SACs@1T-WS_2	2.0 wt.%	185	61	4
Ir_1@Co/NC	2.2 wt.%	60	119	5
Pt@PCM	0.53 wt.%	106	65.3	6
Pt/NPSSF	10 wt.%	71.2	49.85	7
Pt/rGO/GCE	1.00 wt.%	~90	33	8
Pt@PDG_4	6.97 wt%	70	26.52	9
Pt/h-BN(2:1)	-	70.3	34	10
900-nm Pt nanopillar	-	78	71	11
Pt-Mo_2C/TiO_2 NTAs	-	67	39.3	12
Pt/V_2CT_x	17.4 wt%	67	20.6	13
Ni@C-10	0.49 wt%	40	31.7	14
MoS_2@Pt-3	0.26 at% (2.46 wt%)	70	36	15
Pt NP/m-WO_{3-x}	-	150	-	16
Ru@WNO-C	0.9 wt%	172	38.9	17

Table S3. Comparison of HER performance in alkaline media for Pt/CoP with the noble-metal based catalysts.

Catalysts	**Loading of noble metal**	**η_{10} (mV)**	**Tafel slope (mV dec^{-1})**	**Reference**
Pt/CoP	0.12 at.%	16	72.5	This work
Pt/NPSSF	-	71.2	76.8	7
Pt@PDG_4	6.97 wt%	55	95	9
450-nm Pt nanopillar	-	78	59	11
Ru@WNO-C	0.9 wt%	24	39.7	17
PtPd@NLS	2.05 wt%	46	124	18
Pt/$Ni(OH)_2$-nickel foam	-	38	17	19
Pt/Fe-NF	2.050 wt%	59.9	40	20
Pt NC/N-graphene-2	5.0 wt%	24	28	21
Pt/$Ni(OH)_2$	-	25.9	37.6	22
Pt-MoS_2	19.4 at.%	120	28	23
Pt@PDG_4	1.0 at.%	55	79.2	24
Pt@MTO-S	-	73	28	25
$PtNi_5$-0.3	18.2 wt.%	26.8	19.2	26
Pt/NiRu-OH	1.6 at.%	38	39	27
Pt-V_2CT_x	0.88 wt.%	68.1	98.6	28

Reference

1 A. Guha, T.V. Vineesh, A. Sekar, S. Narayanaru, M. Sahoo, S. Nayak, S. Chakraborty and T.N. Narayanan, *ACS Catal.*, 2018, **8**, 6636–6644.

2 H. Yu, Y. Xue, B. Huang, L. Hui, C. Zhang, Y. Fang, Y. Liu, Y. Zhao, Y. Li, H. Liu and Y. Li, *IScience.*, 2019, **11**, 31–41.

3 Q.-Q. Yan, D.-X. Wu, S.-Q. Chu, Z.-Q. Chen, Y. Lin, M.-X. Chen, J. Zhang, X.-J. Wu and H.-W. Liang, *Nat. Commun.*, 2019, **10**, 4977.

4 A. Han, X. Zhou, X. Wang, S. Liu, Q. Xiong, Q. Zhang, L. Gu, Z. Zhuang, W. Zhang, F. Li, D. Wang, L.-J. Li and Y. Li, *Nat. Commun.*, 2021, **12**, 709.

5 W. Lai, L. Zhang, W. Hua, S. Indris, Z. Yan, Z. Hu, B. Zhang, Y. Liu, L. Wang, M. Liu, R. Liu, Y. Wang, J. Wang, Z. Hu, H. Liu, S. Chou and S. Dou, *Angew. Chem. Int. Ed.*, 2019, **58**, 11868–11873.

6 H. Zhang, P. An, W. Zhou, B.Y. Guan, P. Zhang, J. Dong and X.W. (David) Lou, *Sci. Adv.*, 2018, **4**, eaao6657.

7 Y. Tan, Y.K. Wei, K.X. Liang, L.Y. Wang and S.H. Zhang, *Int. J. Hydrogen Energy*, 2021, **46**, 26340–26346.

8 S. Ghasemi, S.R. Hosseini and S. Nabipour, *J. Iran. Chem. Soc.*, 2019, **16**, 101–109.

9 Z.K. Li, F. Han, Z.W. Liu, Q.C. Peng, Q.D. Wang, M.M. Sun and G.J. Kang, *New J. Chem.*, 2021, **45**, 21670–21675.

10 A. Guha, T.V. Vineesh, A. Sekar, S. Narayanaru, M. Sahoo, S. Nayak, S. Chakraborty and T.N. Narayanan, *ACS Catal.*, 2018, **8**, 6636–6644.

11 H.E. Cheng, W.L. Li and Z.P. Yang, *Int. J. Hydrogen Energy*, 2019, **44**, 30141–30150.

12 Y.L. Liu, L.L. Wan, J. Wang, L. Cheng, R.S. Chen and H.W. Ni, *Appl. Surf. Sci.*, 2020, **509**, 144679.

13 J.P. Wang, Y.F. Guan, Q. Zhang, H. Zhu, X.K. Li, Y.J. Li, Z.J. Dong, G.M. Yuan and Y. Cong, *Appl. Surf. Sci.*, 2022, **582**, 152481.

14 Y.P. Xiao, W.J. Wang, T.L. Li, Y.Y. Mao and C.L. Liu, *Electrochim. Acta*, 2021, **386**, 138406.

15 X.Y. Xu, X.F. Dong, Z.J. Bao, R. Wang, J.G. Hu and H.B. Zeng, *J. Mater. Chem. A*, 2017, **5**, 22654–22661.

16 J. Park, S. Lee, H.-E. Kim, A. Cho, S. Kim, Y.J. Ye, J.W Han, H. Lee, J.H. Jang and J. Lee, *Angew. Chem. Int. Ed.*, 2019, **58**, 16038–16042.

17 G. Meng, H. Tian, L.X. Peng, Z.H. Ma, Y.F. Chen, C. Chen, Z.W. Chang, X.Z. Cui and J.L. Shi, *Nano Energy*, 2021, **80**, 105531.

18 L. Huang, Y. Hou, Z. Yu, Z. Peng, L. Wang, J. Huang, B.G. Zhang, L. Qian, L.D. Wu and Z.C. Li, *Int. J. Hydrogen Energy*, 2017, **42**, 9458–9466.

19 H.-E. Cheng, S.-Y. Lin and D.-C. Tian, *J. Electrochem. Soc.*, 2014, **161**, E202–E206.

20 L.R. Huang, Y.P. Hou, Z.B. Yu, Z.B. Peng, L. Wang, J. Huang, B.G. Zhang, L. Qian, L.D. Wu and Z.C. Li, *Int. J. Hydrogen Energy*, 2017, **42**, 9458–9466.

21 B.B. Jiang, F. Liao, Y.Y. Sun, Y.F. Cheng and M.W. Shao, *Nanoscale*, 2017, **9**, 10138–10144.

22 Y.F. Gu, Y.Q. Wang, J.H. Shi, M.R. Yang, Y.C. Rui, W. An and Y. Men, *Int. J. Hydrogen Energy*, 2020, **45**, 27067–27077.

23 Y.L. Liao, C.J. Zhang, J. Ji, P. Jin and X.M. Zhou, *ChemNanoMat*, 2020, **6**, 435–441.

24 Z.K. Li, F. Han, Z.W. Liu, Q.C. Peng, Q.D. Wang, M.M. Sun and G.J. Kang, *New J. Chem.*, 2021, **45**, 21670–21675

25 P. Bhanja, B. Mohanty, A.K. Patra, S. Ghosh, B.K. Jena and A. Bhaumik, *ChemCatChem*, 2019, **11**, 583–592.

26 C. Zhang, X. Liang, R.N. Xu, C.N. Dai, B. Wu, G.Q. Yu, B.H. Chen, X.L. Wang and N. Liu, *Adv. Funct. Mater.*, 2021, **31**, 2008298.

27 D. Li, X.F. Chen, Y.Z. Lv, G.Y. Zhang, Y. Huang, W. Liu, Y. Li, R.S. Chen, C. Nuckolls and H.W. Ni, *Appl. Catal. B Environ.*, 2020, **269**, 118824.

28 S. Park, Y.L. Lee, Y. Yoon, S.Y. Park, S. Yim, W. Song, S. Myung, K.S. Lee, H. Chang, S.S. Lee and K.S. An, *Appl. Catal. B Environ.*, 2022, **304**, 120989.

29 Z. Chen, D. Cummins, B.N. Reinecke, E. Clark, M.K. Sunkara and T.F. Jaramillo, *Nano Lett.*, 2011, **11**, 4168–4175.

30 J.D. Benck, Z.B. Chen, L.Y. Kuritzky, A.J. Forman and T.F. Jaramillo, *ACS Catal.*, 2012, **2**, 1916–1923.

31 J. Kibsgaard and T.F. Jaramillo, *Angewandte Chemie*, 2014, **126**, 14661–14665.

32 Y. Li, J. Hu, M.K. Zhang, W.Y. Gou, S. Zhang, Z. Chen, Y.Q. Qu and Y.Y. Ma, *Nat. Commun.*, 2021, **12**, 3502

33 J.Y. Li, Y. Tan, M.K. Zhang, W.Y. Gou, S. Zhang, Y.Y. Ma, J. Hu and Y.Q. Qu, *ACS Energy Lett.*, 2022, **7**, 1330–1337.